Wavenumber-Domain CRB Optimization for CAPA-Aided Near-Field Sensing

Hao Jiang*, Zhaolin Wang*, Yuanwei Liu†, and Arumugam Nallanathan*
*Queen Mary University of London, London, U.K.
†The University of Hong Kong, Hong Kong.
E-mail: {hao.jiang, zhaolin.wang}@qmul.ac.uk; yuanwei@hku.hk; a.nallanathan@qmul.ac.uk

***Abstract*—A Cramér-Rao bound (CRB) minimization framework for continuous aperture arrays (CAPAs) is proposed in this work. Specifically, the wavenumber-domain method is adopted to discretize the continuous current density function on the transmit CAPA. Based on this, the CRB is derived for monostatic target positioning in the near-field region. The Green's function inherently captures the distance dimension, enabling both angle and distance estimation. To enhance sensing performance, a CRB minimization problem is formulated under the unit-power constraint. Thanks to the discretization in the wavenumber domain, the optimization can be conducted over discrete basis function coefficients, instead of a continuous current density function. Consequently, a manifold-based gradient descent method is employed. Simulation results showcase the effectiveness of the proposed method and demonstrate the CRB performance of CAPAs in the near-field monostatic sensing scenario.**

I. Introduction

Since the first-generation (1G) communication networks were introduced in the 1980s, communication functionalities have been extensively explored and completely transformed people's daily lives. With the commercialization of the fifth generation (5G) in recent years, the sensing functionality of wireless signals has attracted significant attention from both academia and industry [1], [2].

To enhance the sensing performance, multiple-input and multiple-output (MIMO) is promising as an enabling technology, as it can provide high sensing resolution by emitting pencil-like narrow beams. In recent years, the adoption of high-frequency bands and extremely large-aperture aperture arrays (ELAAs) has further expanded the potential of MIMO sensing. Specifically, with high carrier frequencies and larger aperture sizes, the near-field region can be extended to tens or even hundreds of meters, thereby leading to non-negligible spherical wave propagation. Due to the curvature of impinging signals in the near field, the phases of signals are non-uniformly distributed across the receiving antenna array. Leveraging this feature, signals arriving from the same angle but originating at different distances can be distinguished, thus adding an additional distance dimension to the conventional far-field angle-only sensing. To further improve the sensing capability of MIMO, more antennas are integrated within a given physical size, driving the evolution from massive MIMO to gigantic MIMO [3] and ultimately leading to continuous aperture arrays (CAPAs). Compared to conventional spatially discrete arrays (SPDAs), CAPAs pack an infinite number of antennas within a finite array aperture size, thus forming a spatially continuous antenna aperture. With its continuous placement of antennas, CAPA is a promising candidate to fulfill the high spectral efficiency and high-accuracy sensing requirements of the upcoming 6G technologies [4]. In practice, antenna society has developed many prototypes of near-continuous aperture arrays, such as optically driven tightly coupled arrays in [5] and interdigital transducer-based grating antennas in [6].

Compared to the fruitful research endeavors in the communication functionality of CAPAs [4], the sensing functionality remains underexplored. Most existing studies derive fixed CRB based on predefined continuous source current functions, without considering CRB optimization [7]–[9]. However, CRB optimization is important in enhancing the sensing performance, as revealed by research on the SPDA-aided sensing cases [10]. Unlike SPDA cases, the continuous nature of current density functions makes optimization intractable. Moreover, sensing requires handling continuous current functions for both probing signal transmission and echo reception, further complicating CRB optimization. As a remedy, the authors in [11], [12] proposed a wavenumber-domain sampling method that can discretize the continuous current density function to discrete samples, thus enabling optimization. Inspired by this wavenumber-domain method, we first derive the CRB expression based on the wavenumber-domain sampling of the current. Then, a manifold-based gradient descent method is employed to minimize CRB under the unit-power constraint. Finally, numerical results are presented to verify the derivations and the effectiveness of the proposed method.

Notations: Scalars, vectors, and matrices are denoted by the lower-case, bold-face lower-case, and bold-face upper-case letters, respectively. $\Re\{(\cdot)\}$ and $\Im\{(\cdot)\}$ are the operations to extract the real and imaginary parts of $(\cdot)$. $\mathrm{Tr}\{(\cdot)\}$, $(\cdot)^{\intercal}$, $(\cdot)^*$, $(\cdot)^{\mathrm{H}}$, and $[\cdot]^{-1}$ represent the trace, transpose, conjugate, conjugate transpose, and matrix inversion operations, respectively. $\mathbb{R}^{M\times N}$ and $\mathbb{C}^{M\times N}$ denote the $M\times N$ real and imaginary matrix space. $[(\cdot)]_{ij}$ means to take the (i,j)-th entry of matrix/vector $(\cdot)$. $\mathrm{j}=\sqrt{-1}$ is the imaginary unit.

II. System Model

The CAPA-aided near-field sensing framework is shown in Fig. 1, where a base station equipped with linear CAPAs

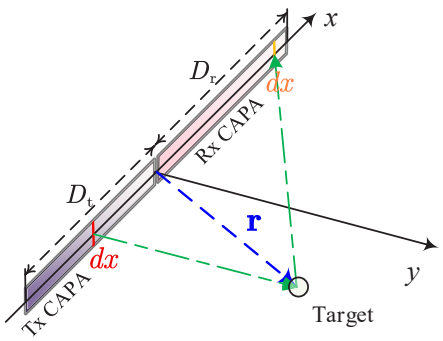

Fig. 1: An illustration of the CAPA-aided single-target positioning system model in the near-field region.

positions a single point-like target in a monostatic manner [1]. This system aims to estimate the position of the target via probing transmissions and echo receptions. Specifically, the BS will send the probing signal to the target using Tx-CAPA while receiving the reflected echo signal by Rx-CAPA. The whole system is located on the XOY plane, and the coordinate origin is set at the center of the Tx-CAPA and Rx-CAPA. The linear Tx-CAPA and Rx-CAPA are placed along the x-axis, whose lengths are specified by D_{t} and D_{r}, respectively. We assume that the target is located within the radiating near-field region of the BS.

A. Spatial-Domain Signal Model

Without loss of generality, the coordinate region of the Tx-CAPA and Rx-CAPA can be specified by

$$\mathcal{D}_{\mathrm{t}} = \left\{ \mathbf{p} \triangleq [p_x, p_y]^{\intercal} : -D_{\mathrm{t}} \le p_x \le 0,\ \ p_y = 0 \right\},$$
$$\mathcal{D}_{\mathrm{r}} = \left\{ \mathbf{q} \triangleq [q_x, q_y]^{\intercal} : 0 \le q_x \le +D_{\mathrm{r}},\ \ q_y = 0 \right\}.$$

It is noted that, due to $p_y = q_y = 0$, the source currents and the channel responses do not vary concerning the y-axis. The location of the sensing target is specified by $\mathbf{r} \triangleq [r_x, r_y]^{\intercal} \in \mathbb{R}^{2\times 1}$. Building on the above, the scalar green's function $g(\cdot,\cdot)$ is specified by [14]:

$$g(\mathbf{y}, \mathbf{x}) = \frac{\mathrm{j}\eta_0 k_0 \mathrm{e}^{-\mathrm{j}k_0\|\mathbf{v}\|_2}}{4\pi \|\mathbf{v}\|_2}, \tag{1}$$

wherein $\mathbf{v} \triangleq \mathbf{y} - \mathbf{x}$ is the vector from the source at $\mathbf{x}$ to the destination at $\mathbf{y}$, $\eta_0 = 120\pi$ denotes the intrinsic impedance of free space, and $k_0 = 2\pi/\lambda$ denotes the wavenumber with λ being the carrier wavelength. This function describes a mapping from a scalar source current $s(\mathbf{p})$ at position $\mathbf{p}$ to an induced scalar radiating field $e(\mathbf{q})$ at position $\mathbf{q}$. Considering both the probing signal transmission and the echo signal reception, we will present the modeling of the round-trip channel in what follows. As illustrated in Fig. 1, an arbitrary length infinitesimal at $\mathbf{p}$ on Tx-CAPA, i.e., $dx \in \mathcal{D}_{\mathrm{t}}$ emits an EM signal according to the source current function, which is then reflected by the target and received by a length infinitesimal at $\mathbf{q}$ on Rx-CAPA, i.e., $dx \in \mathcal{D}_{\mathrm{r}}$ as echo signal. Given the reciprocity theorem in [15], the coupling response (or scattering response) can be expressed as

$$c(\mathbf{n}, \mathbf{r}, \mathbf{m}) = \alpha\delta(\mathbf{r} - \mathbf{n})\delta(\mathbf{r} - \mathbf{m}), \tag{2}$$

where $\alpha \in \mathbb{C}$ denotes the attenuation and polarization on the target, and $\delta(\cdot)$ is the Dirac function. Hence, the round-trip channel can be expressed as

$$\begin{aligned} h(\mathbf{q}, \mathbf{p}) &= \iint_{\mathcal{A}} g(\mathbf{q}, \mathbf{n})\, c(\mathbf{n}, \mathbf{r}, \mathbf{m}) g(\mathbf{m}, \mathbf{p})\, d\mathbf{n} d\mathbf{m} \\ &= \iint_{\mathcal{A}} \frac{\mathrm{j}\eta_0 k_0 \mathrm{e}^{-\mathrm{j}k_0\|\mathbf{q}-\mathbf{n}\|_2}}{4\pi \|\mathbf{q}-\mathbf{n}\|_2} \alpha\delta(\mathbf{r}-\mathbf{n})\delta(\mathbf{r}-\mathbf{m}) \\ &\qquad \times \frac{\mathrm{j}\eta_0 k_0 \mathrm{e}^{-\mathrm{j}k_0\|\mathbf{m}-\mathbf{p}\|_2}}{4\pi \|\mathbf{m}-\mathbf{p}\|_2} d\mathbf{n} d\mathbf{m} \\ &\overset{(a)}{=} \alpha c \frac{\mathrm{e}^{-\mathrm{j}k_0\|\mathbf{q}-\mathbf{r}\|_2}}{\|\mathbf{q}-\mathbf{r}\|_2} \frac{\mathrm{e}^{-\mathrm{j}k_0\|\mathbf{r}-\mathbf{p}\|_2}}{\|\mathbf{r}-\mathbf{p}\|_2}, \end{aligned} \tag{3}$$

where $c \triangleq (\mathrm{j}k_0\eta_0/(4\pi))^2$, $\mathcal{A}$ denotes the entire free space, and (a) is obtained using the property of the Dirac function, Denoting $\mathbf{k} \triangleq \mathbf{q} - \mathbf{r}$ and $\boldsymbol{\kappa} \triangleq \mathbf{r} - \mathbf{p}$, the transmit and receive array response of the target can be expressed as

$$a_{\mathrm{t}}(\mathbf{k}) \triangleq \frac{1}{\|\mathbf{k}\|_2} e^{-\mathrm{j}k_0\|\mathbf{k}\|_2}, \tag{4}$$
$$a_{\mathrm{r}}(\boldsymbol{\kappa}) \triangleq \frac{1}{\|\boldsymbol{\kappa}\|_2} e^{-\mathrm{j}k_0\|\boldsymbol{\kappa}\|_2}. \tag{5}$$

According to [7] and [8], the electronic field at the receiver $e(\mathbf{q})$ induced by a current density at the transmitter $j(\mathbf{p})$ can be bridged by the Green's function. As a result of the adaptation of the scalar Green's function in (1), the received echo signal $y(\mathbf{q})$ at Rx-CAPA in the presence of noise can be expressed as

$$y(\mathbf{q}) = e(\mathbf{q}) + n(\mathbf{q}), \tag{6}$$

where the excited electric filed $e(\mathbf{q})$ is defined by

$$e(\mathbf{q}) \triangleq \int_{\mathcal{D}_{\mathrm{t}}} h(\mathbf{q}, \mathbf{p})\, j(\mathbf{p}) d\mathbf{p} = \int_{-D_{\mathrm{t}}}^{0} h(q_x, p_x)\, j(p_x) dp_x. \tag{7}$$

Moreover, the noise term $n(\mathbf{q}) \in \mathbb{C}$ with $\mathbf{q} \in \mathcal{D}_{\mathrm{r}}$ follows a spatially uncorrelated zero-mean complex Gaussian process. The correlation function of this process is demonstrated by

$$\mathbb{E}\{n(\mathbf{q}) n^{\mathrm{H}}(\mathbf{q}')\} = \sigma^2 \delta(\mathbf{q} - \mathbf{q}'), \tag{8}$$

where σ^2 denotes the power angular density. Here, a spatially white noise model is adopted for simplicity [4]. It is worth noting that the term $\delta(\mathbf{q} - \mathbf{q}')$ in (8) reveals that the noise is uncorrelated across different points $\mathbf{q}$ and $\mathbf{q}'$ on Rx-CAPA. Besides, we consider unit power current density function and add the transmit power term into $h(\mathbf{p}, \mathbf{q})$ by $c_0 = \sqrt{P}c$.

[1]For the mutual coupling issues incurred by the ultra-dense arrangement of antennas, readers are encouraged to refer [13]. This paper deals with the ideal scenario, highlighting the performance upper bound of CAPA.

B. Wavenumber-Domain Signal Model

Although (7) discloses the relationship between transmission and reception, the continuous nature renders such an expression less tractable in analysis and optimization. To address this issue, the wavenumber-domain method is widely used to discretize (7) using the sampling technique in the wavenumber domain. Specifically, the steps for the wavenumber-domain analysis are: 1) expanding $j(\mathbf{p})$ using two-dimensional Fourier space series at the transmit end, and 2) projecting $e(\mathbf{q})$ onto a finite-dimensional space spanned by Fourier basis functions. Accordingly, we first express the continuous current density function $j(\mathbf{p})$ as a weighted summation of basis functions $\{i_x \in \mathcal{K}_\mathrm{t} : \phi_{i_x}(\mathbf{p}) \in \mathbb{C}\}$ with weights $\{i_x \in \mathcal{K}_\mathrm{t} : \vartheta_{i_x} \in \mathbb{C}\}$, in which $\mathcal{K}_\mathrm{t}$ denotes the index set for discrete basis functions. Therefore, the current density function can be expanded as

$$j(\mathbf{p}) = \sum\nolimits_{i_x \in \mathcal{K}_\mathrm{t}} \vartheta_{i_x} \phi_{i_x}(\mathbf{p}), \tag{9}$$

where the weight ϑ_{i_x} and the basis function $\phi_{i_x}(\mathbf{p})$ are respectively given by

$$\vartheta_{i_x} = \frac{1}{\sqrt{D_\mathrm{t}}} \int_{\mathcal{D}_\mathrm{t}} j(\mathbf{p}) \phi_{i_x}^*(\mathbf{p})\, d\mathbf{p}, \tag{10}$$

$$\phi_{i_x}(\mathbf{p}) = \frac{1}{\sqrt{D_\mathrm{t}}} \exp\left\{\mathrm{j}\mathbf{k}_{i_x}^\intercal \mathbf{p}\right\}. \tag{11}$$

Here, $\mathbf{k}_{i_x}$ denotes the discrete version of $\mathbf{k}$ obtained by wavenumber-domain sampling and can be defined by $\mathbf{k}_{i_x} = [2\pi i_x / D_\mathrm{t}, 0]^\intercal \in \mathbb{R}^{2\times 1}$. Here, $\mathbf{k}$ is sampled along the x-axis with an interval of $2\pi/D_\mathrm{t}$, also known as spatial frequency. Since the evanescent near-field region is excluded in our system model, the entries of $\mathbf{k}_{i_x}$ are confined by $\|\mathbf{k}_{i_x}\|_2 \le k_0$. Therefore, the index set can be expressed as

$$\mathcal{K}_\mathrm{t} \triangleq \left\{ i_x \in \mathbb{Z} : (2\pi i_x / D_\mathrm{t})^2 \le 4\pi^2/\lambda^2 \right\}. \tag{12}$$

By doing so, we can approximate the continuous current density function with finite basis functions. In this case, the excited electric field $e(\mathbf{q})$ can be expressed as

$$\begin{aligned} e(\mathbf{q}) &= \int_{\mathcal{D}_\mathrm{t}} h(\mathbf{q},\mathbf{p})\, j(\mathbf{p}) d\mathbf{p} \\ &\approx \int_{\mathcal{D}_\mathrm{t}} h(\mathbf{q},\mathbf{p}) \sum\nolimits_{i_x \in \mathcal{K}_\mathrm{t}} \vartheta_{i_x} \phi_{i_x}(\mathbf{p}) d\mathbf{p} \\ &= \sum\nolimits_{i_x \in \mathcal{K}_\mathrm{t}} \left(\int_{\mathcal{D}_\mathrm{t}} h(\mathbf{q},\mathbf{p})\, \phi_{i_x}(\mathbf{p}) d\mathbf{p} \right) \vartheta_{i_x} \\ &= \sum\nolimits_{i_x \in \mathcal{K}_\mathrm{t}} \mathscr{H}(-\mathbf{k}_{i_x}) \vartheta_{i_x}, \end{aligned} \tag{13}$$

where $\mathscr{H}(-\mathbf{k}_{i_x}) = \mathscr{F}\{h(\mathbf{q},\mathbf{p})\} \mid_{-\mathbf{k}_{i_x}}$ denotes the spatial Fourier transformation results evaluated at spatial frequency $-\mathbf{k}_{i_x}$. From the optimization perspective, we can manipulate $\{\vartheta_{i_x}\}_{i_x \in \mathcal{K}_\mathrm{t}}$ to design favorable $e(\mathbf{q})$.

III. Problem Formulation

To characterize the sensing performance, we adopt CRB as the performance metric, which provides a lower bound on the variance of the unbiased estimator and is widely used. The objective of optimization is to minimize the CRB to enhance the estimation accuracy. In the following, we will present the derivation of CRB and formulate the resultant optimization problem.

A. Wavenumber-Domain CRB Derivations

Given that the position and the reflection coefficient of the sensing target need to be estimated, the unknown parameter vector $\boldsymbol{\xi}$ can be expressed as $\boldsymbol{\xi} = [\mathbf{r}^\intercal, \boldsymbol{\alpha}^\intercal]^\intercal \in \mathbb{R}^{4\times 1}$, where $\boldsymbol{\alpha} \triangleq [\Re\{\alpha\}, \Im\{\alpha\}]^\intercal$ contains the real and imaginary parts of the reflection coefficient of the target. To derive CRB, we first calculate the Fisher information matrix (FIM) for estimating $\boldsymbol{\xi}$, which is given by a partitioned matrix as

$$\mathbf{F}_{\boldsymbol{\xi}} = \begin{bmatrix} \mathbf{F}_{\mathbf{rr}} & \mathbf{F}_{\mathbf{r}\boldsymbol{\alpha}} \\ \mathbf{F}_{\mathbf{r}\boldsymbol{\alpha}}^\intercal & \mathbf{F}_{\boldsymbol{\alpha}\boldsymbol{\alpha}} \end{bmatrix}. \tag{14}$$

According to [7], we have that $\mathbf{F}_{\mathbf{rr}}$, $\mathbf{F}_{\boldsymbol{\alpha}\boldsymbol{\alpha}}$, and $\mathbf{F}_{\mathbf{r}\boldsymbol{\alpha}}$ are originally expressed as:

$$[\mathbf{F}_{\mathbf{rr}}]_{m,n} = \frac{2}{\sigma^2} \int_0^{D_\mathrm{r}} \Re\left\{ \frac{\partial e(q_x)}{\partial [\mathbf{r}]_m} \frac{\partial e^*(q_x)}{\partial [\mathbf{r}]_n} \right\} dq_x, \tag{15}$$

$$[\mathbf{F}_{\boldsymbol{\alpha}\boldsymbol{\alpha}}]_{m,n} = \frac{2}{\sigma^2} \int_0^{D_\mathrm{r}} \Re\left\{ \frac{\partial e(q_x)}{\partial [\boldsymbol{\alpha}]_m} \frac{\partial e^*(q_x)}{\partial [\boldsymbol{\alpha}]_n} \right\} dq_x, \tag{16}$$

$$[\mathbf{F}_{\mathbf{r}\boldsymbol{\alpha}}]_{m,n} = \frac{2}{\sigma^2} \int_0^{D_\mathrm{r}} \Re\left\{ \frac{\partial e(q_x)}{\partial [\mathbf{r}]_m} \frac{\partial e^*(q_x)}{\partial [\boldsymbol{\alpha}]_n} \right\} dq_x. \tag{17}$$

In what follows, we will present the calculation of each partial derivative term. According to (10), (11), and (13), the partial derivatives with respect to $\mathbf{r}$ can be derived as follows:

$$\begin{aligned} \nabla_{\mathbf{r}} e(\mathbf{q}) &= \nabla_{\mathbf{r}} \left\{ \sum\nolimits_{i_x \in \mathcal{K}_\mathrm{t}} \left(\int_{\mathcal{D}_\mathrm{t}} h(\mathbf{q},\mathbf{p})\, \phi_{i_x}(\mathbf{p}) d\mathbf{p} \right) \vartheta_{i_x} \right\} \\ &= \sum\nolimits_{i_x \in \mathcal{K}_\mathrm{t}} \left(\int_{\mathcal{D}_\mathrm{t}} \nabla_{\mathbf{r}} h(\mathbf{q},\mathbf{p})\, \phi_{i_x}(\mathbf{p}) d\mathbf{p} \right) \vartheta_{i_x} \\ &= \sum\nolimits_{i_x \in \mathcal{K}_\mathrm{t}} \mathscr{H}'(-\mathbf{k}_{i_x}) \vartheta_{i_x}, \end{aligned} \tag{18}$$

in which $\mathscr{H}'(-\mathbf{k}_{i_x}) = \mathscr{F}\{\dot{h}_{\mathbf{r}}\} \mid_{-\mathbf{k}_{i_x}}$ denotes the Fourier transform of $\dot{h}_{\mathbf{r}_n}$ evaluated at $-\mathbf{k}_{i_x}$, and

$$\begin{aligned} \dot{h}_{\mathbf{r}} &\triangleq \nabla_{\mathbf{r}} h(\mathbf{q},\mathbf{p}) = \nabla_{\mathbf{r}} \left(a_\mathrm{r}(\boldsymbol{\kappa})\, \alpha a_\mathrm{t}(\mathbf{k}) \right) \\ &= \left(\nabla_{\mathbf{r}} a_\mathrm{r}(\boldsymbol{\kappa}) \right) \alpha a_\mathrm{t}(\mathbf{k}) + a_\mathrm{r}(\boldsymbol{\kappa})\, \alpha \left(\nabla_{\mathbf{r}} a_\mathrm{t}(\mathbf{k}) \right). \end{aligned} \tag{19}$$

In (19), $\nabla_{\mathbf{r}} a_\mathrm{r}(\boldsymbol{\kappa})$ and $\nabla_{\mathbf{r}} a_\mathrm{t}(\mathbf{k})$ can be derived as

$$\nabla_{\mathbf{r}} a_\mathrm{t}(\mathbf{k}) = -\frac{\mathbf{r}}{\|\mathbf{k}\|_2^3} \left(1 + \mathrm{j}k_0 \|\mathbf{k}\|_2\right) e^{-\mathrm{j}k_0\|\mathbf{k}\|_2},$$

$$\nabla_{\mathbf{r}} a_\mathrm{r}(\boldsymbol{\kappa}) = \frac{\mathbf{r}}{\|\boldsymbol{\kappa}\|_2^3} \left(1 + \mathrm{j}k_0 \|\boldsymbol{\kappa}\|_2\right) e^{-\mathrm{j}k_0\|\boldsymbol{\kappa}\|_2}.$$

Moreover, the partial derivative with respect to the real and imaginary parts of the reflection coefficient α can be derived through

$$\frac{\partial e(\mathbf{q})}{\partial \Re\{\alpha\}} = \Re\left\{ \sum\nolimits_{i_x \in \mathcal{K}_\mathrm{t}} \mathscr{F}\left\{ \dot{h}_{\Re\{\alpha\}} \right\} \vartheta_{i_x} \right\}, \tag{20}$$

$$\frac{\partial e(\mathbf{q})}{\partial \Im\{\alpha\}} = \Im\left\{ \sum\nolimits_{i_x \in \mathcal{K}_\mathrm{t}} \mathscr{F}\left\{ \dot{h}_{\Im\{\alpha\}} \right\} \vartheta_{i_x} \right\}, \tag{21}$$

where we have

$$\dot{h}_{\Re\{\alpha\}} \triangleq \frac{\partial h\left(\mathbf{q},\mathbf{p}\right))}{\partial \Re\left\{\alpha\right\}} = c_0 a_{\mathrm{r}}\left(\boldsymbol{\kappa}\right) a_{\mathrm{t}}\left(\mathbf{k}\right),$$

$$\dot{h}_{\Im\{\alpha\}} \triangleq \frac{\partial h\left(\mathbf{q},\mathbf{p}\right))}{\partial \Im\left\{\alpha\right\}} = \mathrm{j} c_0 a_{\mathrm{r}}\left(\boldsymbol{\kappa}\right) a_{\mathrm{t}}\left(\mathbf{k}\right).$$

With (18), (20) and (21), the entries of (15), (16), and (17) can be obtained. To deal with the outer integration over the coordinate region of the Rx CAPA, we adopt the Gauss–Legendre integration to evaluate the numerical results, which can replace intractable integrations with weighted summations. Then, on top of $\mathbf{F}_{\boldsymbol{\xi}}$, the CRB matrix for estimating $\boldsymbol{\xi}$ in the discrete case can be written as

$$\mathrm{CRB}\left(\mathbf{F}_{\mathbf{rr}}\right) = \left[\mathbf{F}_{\mathbf{rr}} - \mathbf{F}_{\mathbf{r}\boldsymbol{\alpha}}\mathbf{F}_{\boldsymbol{\alpha}\boldsymbol{\alpha}}^{-1}\mathbf{F}_{\mathbf{r}\boldsymbol{\alpha}}^{\intercal}\right]^{-1}. \tag{22}$$

B. CRB Minimization Problem Formulation

Based on the above derivations, we intend to minimize the CRB to enhance the sensing accuracy while preserving the constraint on the total power budget. Thus, the optimization problem can be formulated as

$$\min_{\boldsymbol{\vartheta}} \ \mathrm{Tr}\left\{\mathrm{CRB}\left(\mathbf{F}_{\mathbf{rr}}\right)\right\} \tag{23a}$$

$$\text{s.t.} \ \sum\nolimits_{i_x \in \mathcal{K}_{\mathrm{t}}} \left|\vartheta_{i_x}\right|^2 = 1, \tag{23b}$$

where $\boldsymbol{\vartheta} \triangleq \left\{\vartheta_{i_x}\right\}_{i_x \in \mathcal{K}_{\mathrm{t}}}$ denotes the Fourier coefficients vector. According to (23a), both the objective function and constraint are defined by the discrete Fourier coefficients obtained through wavenumber-domain sampling, rather than the intractable continuous source current function. To handle the unit-power constraint in (23b), we apply the manifold gradient descent method for efficient optimization, which will be detailed in Section IV.

IV. Methodology

According to (23a), we aim to design the discrete weights, i.e., $\boldsymbol{\vartheta}$, rather than a continuous current density function $j(\mathbf{p})$ directly. To simply the optimization problem, the constraint (23b) can be recast as

$$\left\|\boldsymbol{\vartheta}\right\|_2^2 = \left\|\mathrm{Vect}\left\{\left\{\vartheta_{i_x}\right\}_{i_x \in \mathcal{K}_{\mathrm{t}}}\right\}\right\|_2^2 = 1. \tag{24}$$

Therefore, the feasible set of the original optimization problem is now constrained on the surface of the sphere with a unit radius. Motivated by this, we exploit the Riemannian manifold optimization technique. Specifically, we define the sphere manifold as follows:

$$\mathcal{M} \triangleq \left\{\boldsymbol{\vartheta} \in \mathbb{C}^{|\mathcal{K}_{\mathrm{t}}|\times 1} : \boldsymbol{\vartheta}^{\mathrm{H}}\boldsymbol{\vartheta} = 1\right\}, \tag{25}$$

where $|\mathcal{K}_{\mathrm{t}}|$ represents the cardinality of set $\mathcal{K}_{\mathrm{t}}$. Therefore, by performing gradient descent on $\mathcal{M}$, the original problem can be converted into an unconstrained counterpart. In this case, the gradient descent method can be utilized to minimize the objective function. To enable gradient descent, we first need to define the gradients on $\mathcal{M}$. Based on the definition of inner product presented by (25), the tangent space is defined by

$$\mathcal{T}_{\boldsymbol{\vartheta}}\mathcal{M} \triangleq \left\{\boldsymbol{\eta} \in \mathbb{C}^{|\mathcal{K}_{\mathrm{t}}|\times 1} : \boldsymbol{\eta}^{\mathrm{H}}\boldsymbol{\vartheta} = 0\right\}, \tag{26}$$

Algorithm 1: Manifold-Based CRB minimization

Input: Initial guess $\boldsymbol{\vartheta}_0$, round-trip channel $h(\mathbf{q},\mathbf{p})$, error-tolerant threshold δ, maximum number of iterations K, sampled wavenumber-domain vectors and associated weights, and initial step index $k = 0$.

Output: The optimized weight vector $\boldsymbol{\vartheta}$.

// Prerequisite Step:

Calculate the initial gradient descent direction via $\mathbf{d}_0 = -\mathrm{grad}_{\boldsymbol{\vartheta}}\left\{u\left(\boldsymbol{\vartheta}_0\right)\right\}$ according to (27) ;

// Preforming Conjugate Gradient Descent:

while *(*$\left\|u(\boldsymbol{\vartheta}_{k+1}) - u(\boldsymbol{\vartheta}_k)\right\|_2 \geq \delta$ *and* $k < K$*) or* $k = 0$ **do**

  Find the step size α_k by Armijo backtracking line search;

  Find the next point $\boldsymbol{\vartheta}_{k+1}$ via traction $\boldsymbol{\vartheta}_{k+1} = \mathrm{retr}_{\boldsymbol{\vartheta}}\left\{\alpha_k \mathbf{d}_k\right\}$ according to (28);

  Compute the Riemannian gradient at point $\boldsymbol{\vartheta}_{k+1}$ via $\boldsymbol{\eta}_{k+1} = \mathrm{grad}_{\boldsymbol{\vartheta}}\left\{u\left(\boldsymbol{\vartheta}_{k+1}\right)\right\}$;

  Calculate the conjugate direction coefficient β_k;

  Update the search direction via $\mathbf{d}_{k+1} = -\boldsymbol{\eta}_{k+1} + \beta_k \mathrm{trans}_{\boldsymbol{\vartheta}_k \to \boldsymbol{\vartheta}_{k+1}}\left\{\mathbf{d}_k\right\}$;

  Step into the next iteration by $k = k + 1$;

end

return *The optimized weight vector* $\boldsymbol{\vartheta} = \boldsymbol{\vartheta}_k$.

which describes all the vectors perpendicular to $\boldsymbol{\vartheta}$. Then, the Riemanian gradient defined by the steepest direction on $\mathcal{M}$ can be expressed by

$$\mathrm{grad}_{\boldsymbol{\vartheta}}\left\{u\left(\boldsymbol{\vartheta}\right)\right\} = \nabla_{\boldsymbol{\vartheta}} u\left(\boldsymbol{\vartheta}\right) - \boldsymbol{\vartheta}\left(\boldsymbol{\vartheta}^{\mathrm{H}}\nabla_{\boldsymbol{\vartheta}} u\left(\boldsymbol{\vartheta}\right)\right) = \boldsymbol{\eta}, \tag{27}$$

where $u\left(\boldsymbol{\vartheta}\right) \triangleq \mathrm{Tr}\{\mathrm{CRB}\left(\mathbf{F}_{\mathbf{rr}}\right)\}$. To project the gradients back to $\mathcal{M}$, we define the retraction operator, which can map a search direction $\mathbf{d} = -\alpha\boldsymbol{\eta}$ on the tangent space to the manifold and is characterized by

$$\mathrm{retr}_{\boldsymbol{\vartheta}}\left\{\mathbf{d}\right\} \triangleq \boldsymbol{\vartheta} + \mathbf{d}/\left\|\boldsymbol{\vartheta} + \mathbf{d}\right\|_2, \tag{28}$$

where $\mathbf{d} \in \mathcal{T}_{\boldsymbol{\vartheta}}\mathcal{M}$ and $\alpha > 0$ denotes the step size. Additionally, we need to define a transport operation, which maps two directions of two different tangent spaces and is given by

$$\mathrm{trans}_{\boldsymbol{\vartheta}_k \to \boldsymbol{\vartheta}_{k+1}}\left\{\mathbf{d}_k\right\} = \mathbf{d}_k - \boldsymbol{\vartheta}_{k+1}^{\mathrm{H}}\mathbf{d}_k = \mathbf{d}_{k+1}, \tag{29}$$

where $\mathbf{d}_{k+1}$ and $\mathbf{d}_k$ are two point on $\mathcal{M}$ and $\mathrm{trans}_{\boldsymbol{\vartheta}_k \to \boldsymbol{\vartheta}_{k+1}}\left\{\boldsymbol{\eta}\right\}$ maps the tangent space at $\boldsymbol{\vartheta}_{k+1}$ and $\boldsymbol{\vartheta}_k$ respectively, i.e., $\mathcal{T}_{\boldsymbol{\vartheta}_{k+1}}\mathcal{M}$ and $\mathcal{T}_{\boldsymbol{\vartheta}_k}\mathcal{M}$. Furthermore, we adopt the Polak-Ribière conjugated gradient descent method. Thus, the overall algorithm is summarized in **Algorithm 1**.

V. Simulation Results

In this section, simulation results are presented to verify the derivations and the effectiveness of the proposed algorithms. The coordinate range of Tx-CAPA and Rx-CAPA are specified by $[-1\ \mathrm{m}, 0\ \mathrm{m}]$ and $[0\ \mathrm{m}, 1\ \mathrm{m}]$, respectively. The transmit power and noise power are set to 20 dBm and 0 dBm, respectively. The reflection coefficient is $\alpha = 10 + 10\mathrm{j}$. The carrier frequency is set to 28 GHz. The number of Gaussian-Legendre (GL) points used for numerical integration is set to 300. The maximum number of iterations is set to $K = 50$, with $\delta = 10^{-4}$ being the tolerance threshold.

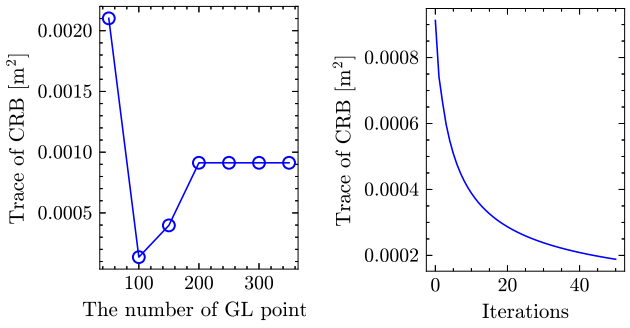

(a) Impact of the number of GL points (b) Convergence behavior

Fig. 2: Illustration of the impact of the number of GL points and the convergence behavior of the proposed algorithm.

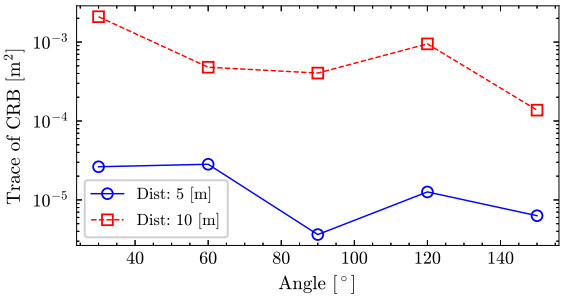

(a) CRB versus angles at different distances

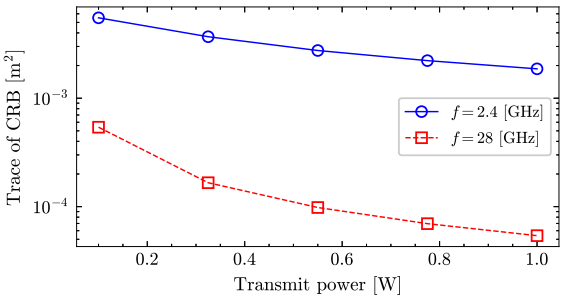

(b) CRB versus transmit power at different carrier frequencies

Fig. 3: Illustration of the achieved CRB versus angle and transmit power.

Fig. 2 shows the impact of the number of GL points and the convergence behavior. It can be observed that the numerical integration converges when the number of GL points is set to 200, which justifies our simulation setups. Then, Fig. 2b illustrates the effectiveness of the proposed manifold gradient-descent for CRB minimization.

In Fig. 3, we investigate the impact of angles and transmit power on the achieved CRB. As shown in Fig. 3a, we place the sensing target at different angles in front of the Rx-CAPA. Two distance settings of 5 m and 10 m are considered. The asymmetry of the curves arises from the non-symmetric placement of the Tx- and Rx-CAPA. Fig. 3b shows that the CRB decreases with increasing transmit power and that higher carrier frequencies further improve CRB performance.

VI. Conclusions

This paper investigated the CRB minimization problem for CAPAs in the near-field monostatic sensing scenario. In particular, to enable optimizations, the wavenumber-domain method is utilized to discretize the continuous current density function on the Tx-CAPA by sampling finite terms from the wavenumber domain. Building on this, CRB is derived based on discrete wavenumber-domain samples. Then, a manifold gradient descent method is applied to minimize CRB, improving sensing performance. Finally, numerical results are presented to confirm the effectiveness of the proposed method.

References

[1] W. Jiang *et al.*, "Terahertz communications and sensing for 6G and beyond: A comprehensive review," *IEEE Commun. Surveys Tut.*, pp. 1–1, 2024.

[2] C.-X. Wang *et al.*, "On the road to 6G: Visions, requirements, key technologies, and testbeds," *IEEE Commun. Surveys Tut.*, vol. 25, no. 2, pp. 905–974, Feb. 2023.

[3] E. Björnson *et al.*, "Enabling 6G performance in the upper mid-band by transitioning from massive to gigantic MIMO," *IEEE Open J. Commun. Soc.*, early access, 2025, doi: 10.1109/OJCOMS.2025.3576931.

[4] Z. Zhang *et al.*, "Pattern-division multiplexing for multi-user continuous-aperture MIMO," *IEEE J. Sel. Areas Commun.*, vol. 41, no. 8, pp. 2350–2366, Apr. 2023.

[5] D. W. Prather *et al.*, "Optically upconverted, spatially coherent phased-array-antenna feed networks for beam-space MIMO in 5G cellular communications," *IEEE Trans. Antennas Propag.*, vol. 65, no. 12, pp. 6432–6443, Dec. 2017.

[6] Y. Yuan and o. Jiang, "Interdigital waveguide grating antenna array for an optical phased array," *Appl. Opt.*, vol. 63, no. 28, pp. 7370–7377, 2024.

[7] A. A. D'Amico *et al.*, "Cramér-Rao bounds for holographic positioning," *IEEE Trans. Signal Process.*, vol. 70, pp. 5518–5532, Nov. 2022.

[8] A. Chen *et al.*, "Cramér-Rao bounds of near-field positioning based on electromagnetic propagation model," *IEEE Trans. Veh. Technol.*, vol. 72, no. 11, pp. 13 808–13 825, Jun. 2023.

[9] ——, "Near-field positioning and attitude sensing based on electromagnetic propagation modeling," *IEEE J. Sel. Areas Commun.*, vol. 42, no. 9, pp. 2179–2195, Jun. 2024.

[10] F. Liu *et al.*, "Cramér-rao bound optimization for joint radar-communication beamforming," *IEEE Trans. Signal Process.*, vol. 70, pp. 240–253, Dec. 2022.

[11] A. Pizzo *et al.*, "Fourier plane-wave series expansion for holographic MIMO communications," *IEEE Trans. Wireless Commun.*, vol. 21, no. 9, pp. 6890–6905, Sept. 2022.

[12] L. Sanguinetti *et al.*, "Wavenumber-division multiplexing in line-of-sight holographic MIMO communications," *IEEE Trans. Wireless Commun.*, vol. 22, no. 4, pp. 2186–2201, Sept. 2023.

[13] A. Pizzo *et al.*, "Mutual coupling in holographic MIMO: Physical modeling and information-theoretic analysis," 2025. [Online]. Available: https://arxiv.org/abs/2502.10209

[14] A. Pizzo, L. Sanguinetti, and T. L. Marzetta, "Spatial characterization of electromagnetic random channels," *IEEE Open J. Commun. Soc.*, vol. 3, pp. 847–866, Apr. 2022.

[15] A. Poon *et al.*, "Degrees of freedom in multiple-antenna channels: a signal space approach," *IEEE Trans. Inf. Theory*, vol. 51, no. 2, pp. 523–536, Feb. 2005.